VELOX - A new thermal infrared imager for airborne remote sensing of cloud and surface properties

Michael Schäfer[1], Kevin Wolf[1,*], André Ehrlich[1], Christoph Hallbauer[2], Evelyn Jäkel[1], Friedhelm Jansen[3], Anna Elizabeth Luebke[1], Joshua Müller[1], Jakob Thoböll[1], Timo Röschenthaler[2], Bjorn Stevens[3], and Manfred Wendisch[1]

[1]Leipzig Institute for Meteorology, University of Leipzig, Germany
[2]*enviscope GmbH*, Frankfurt am Main, Germany
[3]Max Planck Institute for Meteorology, Hamburg, Germany
[*]Now at: Institut Pierre-Simon Laplace, Sorbonne Université, Paris, France

Correspondence: Michael Schäfer (michael.schaefer@uni-leipzig.de)

Abstract. The new airborne thermal infrared (TIR) imager VELOX (Video airbornE Longwave Observations within siX channels) is introduced. The commercial camera system of VELOX covers six spectral bands with center wavelengths between 7.7 μm and 12 μm. VELOX is currently applied on board the German High Altitude and Long Range Research Aircraft (HALO). It observes two-dimensional fields of upward terrestrial spectral radiance with a horizontal spatial resolution of

5 approximately 10 m by 10 m at a target distance of 10 km. Atmospheric temperature values are rather low compared to the original application of the TIR imager system and range close to the detection limit of the sensor. This challenge requires additional calibration efforts to reduce the measurement uncertainties of VELOX. These calibration and correction procedures, including radiometric calibrations, non-uniform corrections, bad-pixel replacements, and window corrections for data collected by VELOX, are presented. First measurements acquired by VELOX during the EUREC[4]A (ElUcidating the RolE of Cloud-

10 Circulation Coupling in ClimAte) campaign are presented, including an analyses of the cloud top brightness temperature, cloud mask/fraction, and cloud top altitude data. They reveal that the cloud top temperature can be resolved with a resolution of better than 0.1 K, which translates into a resolution of approximately 40 m with respect to cloud top altitude.

1 Introduction

Thermal infrared (TIR) imagery is a well established technique to study atmospheric and surface properties from ground,

15 space, and aircraft platforms. Especially for satellite-based instruments, various retrieval techniques were developed to derive cloud properties like cloud coverage, cloud top temperature and height, thermodynamic phase, and particle effective radius or liquid/ice water path (e.g., Brogniez et al., 2003; Chylek et al., 2006; Iwabuchi et al., 2014, 2016; Platnick, 2017; Someya and Imasu, 2018; Frey et al., 2020). Surface property retrievals provide products for the surface typing, surface temperature (Haggerty et al., 2003; Kilpatrick et al., 2015; Fu et al., 2020), or snow grain size (Hori et al., 2006).

20 However, most of the satellite products suffer from a low spatial resolution (often in the range of kilometers), which makes them unable to resolve smaller cloud structures. This may lead to uncertainties in the estimation of, e.g., the cloud radiative

forcing, if the cloud coverage or the cloud top altitude is estimated wrong (Pavolonis and Key, 2003). Often, they also provide a low temporal resolution with overpasses over the same region only once daily or less (polar orbiting satellites). For example, the MODerate resolution Imaging Spectrometer (MODIS) on board of Aqua and Terra provides radiance measurements at

25 several TIR channels, but at 1 km spatial resolution only (Esaias et al., 1998; Platnick, 2017). The Advanced Very High Resolution Radiometer (AVHRR; Cracknell, 1997) multi-purpose imaging instrument has three TIR channels, but also at 1 km spatial resolution only. The Visible Infrared Imaging Radiometer Suite (VIIRS; Justice et al., 2013) provides a TIR band for cloud imagery with comparable higher spatial resolution of up to 375 m. This is topped by the Advanced Spaceborne Thermal Emission and Reflection Radiometer (ASTER) on Terra, which has a TIR channel with even higher spatial resolution of 90 m,

30 but data is not collected continuously (on average only 8 minutes per orbit; Abrams, 2000). However, all the sensors cross the same region on Earth only once or twice per day and are probably close to the end of their lifetime. The Multi-Spectral Imager (MSI) instrument on the proposed Earth Clouds, Aerosol and Radiation Explorer satellite missions (EarthCARE; Illingworth et al., 2015) will provide a much improved replacement for, e.g., MODIS, but as a polar orbiting satellite, it will suffer from similar temporal resolution issues. The Geostationary Operational Environmental Satellite (GOES) provides data with one-

35 minute resolution, but due to its geostationary orbit, the spatial resolution is decreased to kilometer range (Schmit et al., 2018).

To perform cloud and surface observations with higher spatial and temporal resolution and to validate satellite products, airborne thermal sensors and imagers were developed. Notable instruments are the Airborne Visible/Infrared Imaging Spectrometer (AVIS; Oppelt and Mauser, 2007), the enhanced MODIS Airborne Simulator (EMAS-HS; Guerin et al., 2011), or the far infrared radiometer (FIRR; Libois et al., 2016), which helped to develop cloud and surface products based on TIR ob-

40 servations. For the same purpose (increased resolution, satellite validation), airborne imaging spectro-radiometers, radar, and microwave radiometers were developed (e.g., Wirth et al., 2009; Bierwirth et al., 2013; Mech et al., 2014; Ewald et al., 2015; Schnitt et al., 2017; Schäfer et al., 2017) and implemented within the remote sensing package of the High Altitude and LOng Range Research Aircraft (HALO). This sensor package was operated during the Next-generation Aircraft Remote-Sensing for Validation Studies (NARVAL-I, Klepp et al., 2014; Stevens et al., 2019), the NARVAL-II (Stevens et al., 2019), and the North

45 Atlantic Waveguide and Downstream Impact Experiment (NAWDEX, Schäfler et al., 2018) HALO campaigns. The synergy of the HALO remote sensing package was utilized to retrieve various microphysical and macrophysical cloud properties (e.g., Delanoë et al., 2013; Fricke et al., 2014; Wolf et al., 2019).

With respect to clouds, this suite of instruments provides each a different view on the clouds and different sensitivities to the cloud properties. Based on the single-scattering assumption, active radar (e.g., the HALO Microwave Package; HAMP,

50 Mech et al., 2014; Konow et al., 2019) and lidar (e.g., the Water vapor Lidar Experiment in Space; WALES; Wirth et al., 2009) observations are dominated by either large cloud droplets (radar) or small cloud particles (lidar). Passive instruments are sensitive to a larger range of cloud particle sizes and observe radiation that is multiply-scattered or emitted within the cloud. Depending on the wavelength of the reflected solar or emitted thermal radiation, different vertical weightings have to be considered for the interpretation of the retrieved data (e.g., Platnick, 2000). For solar wavelengths, where clouds mostly

55 scatter, the weighting function extends down to the cloud base. In contrast, the emitted thermal radiation is mostly dominated

by the cloud properties at the upper layer (Platnick, 2000). The different vertical weightings highlight the potential of retrieval approaches combining various remote sensing instruments (Schnitt et al., 2017; Wolf et al., 2019; Villanueva et al., 2021).

For satellite observations, combinations of different remote sensing techniques are provided by, e.g., the raDAR/liDAR (DARDAR) cloud classification (Delanoë and Hogan, 2010). These satellite products do not only combine radar and lidar
60   observations, but also consider measurements of the TIR radiation emitted by the clouds at wavelengths between 3.7 µm and 12 µm. Different studies prove the benefit of using TIR radiation for satellite cloud remote sensing applications (e.g., Parol, 1991; Garnier et al., 2012). For example, three-dimensional (3D) radiative effects, which often cause problems in the solar wavelength range, are avoided, or the detection of clouds above bright surfaces (snow, sea ice) becomes possible due to their different temperatures.

65   However, the radiometric calibration of TIR sensors is challenging because the detectors can only register a temperature difference between the target and the sensor temperature itself. Keeping the sensor temperature constant is a major requirement, either realized by cooling systems or by recording the sensor temperature. As this is not always given, many TIR imagers apply on-board calibrations with black bodies.

Here we describe a new temperature-stabilized TIR imager, which measures radiance in six spectral bands in the TIR
70   wavelength range from 7.7 µm to 12.0 µm. It is currently implemented into the instrumentation package of HALO for airborne observations, but can potentially be operated on other airborne platforms and as a ground-based sky imager similar to Schäfer et al. (2013) or Jäkel et al. (2013). Therefore, it supplements the remote sensing package of HALO to achieve a similar combination as in the current A-train and the proposed EarthCARE satellite missions (Illingworth et al., 2015). The imaging sensor of the instrument is commercially available and manufactured by the IRCAM GmbH, Erlangen, Germany. The full
75   system is called VELOX (Video airbornE Longwave Observations within siX channels).

The VELOX instrumentation and system design for airborne operations is presented in Sect. 2, necessary correction procedures with respect to geometric (pixel size and orientation, image shift due to the use of different filters) and radiometric (radiometric calibration, non-uniform correction, bad-pixel replacement, radiometric cross-calibration, and window correction) calibrations are described in Sect. 3. VELOX was used for the first time in the field during the ElUcidating the RolE of Cloud-
80   Circulation Coupling in ClimAte (EUREC4A; Bony et al., 2017; Stevens et al., 2021) expedition, which was carried out in January/February 2020 in the vicinity of Barbados. The data collected during the EUREC[4]A campaign are used in Sect. 4 to demonstrate the capabilities of the new VELOX system. Examples are given for deriving the cloud top brightness temperature, cloud cover, and cloud top altitude.

2   Instrumentation

85   The camera system installed in VELOX comprises two components: a TIR imager (VELOX327k veL), and an infrared thermometer (Heitronics KT19.85II), which serves as a secondary reference. On board HALO, both instruments are installed in a nadir viewing orientation to observe the upward spectral TIR radiance emitted by clouds and surfaces within the large atmospheric spectral window. The TIR imager has a sensor with 640 by 512 spatial pixels providing two-dimensional (2D) images

Table 1. Specifications of the TIR imager (VELOX327k veL) and the infrared thermometer (KT19.85II).

Specification	TIR Imager (VELOX327k veL)	Infrared thermometer (KT19.85II)
Spectral range	7.7 μm to 12.0 μm	9.6 μm to 11.5 μm
Detector technology	Cadmium-Mercury-Telluride	Thermo-electric
Sensor Format	640 x 512 pixels	1 pixel
Field of view (FOV)	35.5° x 28.7°	2.3°
Measurable temperature range	-40°C to 100°C	-50°C to 50°C
Noise equivalent temperature difference (NETD)	40 mK	100 mK
Integration time	5 μs to 150 μs	5 ms
Measurement frequency	100 Hz	20 Hz
Cooling	active (Sterling)	un-cooled
Operation temperature	-15°C to 50°C	-20°C to 70°C
Weight	5 kg	2.35 kg
Power consumption	< 50 W	< 4 W

with a maximum frame rate of 100 Hz. The infrared thermometer is a single sensor radiometer pointing close to the center of
90   the 2D images. The main technical specifications are listed in Tab. 1.

2.1   Spectral channel selection

To fulfill the demands of making the TIR imager a tool for cloud and surface characterization, observations at different wave-
lengths were realized. A synchronously rotating filter wheel, providing six slots for spectral filters, is mounted between the
lens and the detector; it rotates with a frequency of 100 Hz. Four of the six filter-wheel slots are equipped with band-pass and
95   low-pass filters, which are partly adapted to the channels of satellite instruments such as MODIS (Esaias et al., 1998; Platnick,
2017), MSI (Illingworth et al., 2015), VIIRS (Justice et al., 2013), and AVHRR (Cracknell, 1997). The applied filter/channel
assembly is summarized in Tab. 2, listing their respective spectral range and space-borne sensor equivalents. The mean max-
imum transmissivity $\mathcal{T}$ of the single filters is in the range between 0.8 and 0.9 (Tab. 2). The smaller the wavelength range of
the filter, the smaller the signal reaching the detector, which increases the measurement uncertainty. For some applications,
100   such narrow wavelength bands are not needed, e.g., for sea surface temperature or cloud top altitude retrievals. Therefore, two
positions of the filter wheel were equipped with optically transparent ($\mathcal{T} = 0.9395$) windows (Channels 1 and 4 in Tab. 2) for
broadband measurements in the full spectral range covered by the detector (7.7 - 12 μm). These two broadband channels, 1 and
4, are used to derive the sea-surface temperature, cloud top temperature, and cloud top altitude.

Channels 2 and 5 capture the typical spectral behavior of the imaginary part of the refractive index of liquid water and
105   ice. For both, Chylek et al. (2006) revealed that in the wavelength range between 8.5 μm and 10 μm the imaginary part of the
refractive index is rather equal, but shows significantly different slopes at wavelengths between 11 μm and 12 μm. Therefore,

Table 2. List of all VELOX channels. The wavelength ranges (λ) of the narrow-band channels are determined by the center wavelength of the particular filter and its half width. The third column lists the mean maximum transmissivity $\mathcal{T}_{max}$ of the channel filters. According to the wavelength ranges, equivalent MODIS, MSI, VIIRS, and AVHRR bands and center wavelengths are listed.

Channel	VELOX (λ)	$\mathcal{T}_{max}$	MODIS (Band; λ)	MSI (Band; λ)	VIIRS (Band; λ)	AVHRR (Band; λ)
1	7.70 - 12.00 µm	0.94	-	-		-
2	8.65 ± 0.55 µm	0.89	29; 8.55 µm	5; 8.80 µm	M14; 8.55 µm	-
3	10.74 ± 0.39 µm	0.83	31; 11.03 µm	6; 10.80 µm	M15; 10.76 µm	4; 10.8 µm
4	7.70 - 12.00 µm	0.94	-	-	-	-
5	11.66 ± 0.81 µm	0.88	31; 11.03 µm	7; 12.00 µm	I5; 11.45 µm	-
6	12.00 ± 0.50 µm	0.92	32; 12.02 µm	7; 12.00 µm	M16; 12.01 µm	5; 12 µm
KT19	9.60 - 11.50 µm					

those two wavelength regions are suitable to discriminate between liquid water and ice in clouds; they can also be used to derive the cloud effective radius or the liquid water path (Iwabuchi et al., 2016; Someya and Imasu, 2018) by applying the split-window method (McMillin, 1980; Brogniez et al., 2003; Heidinger and Pavalonis, 2009).

110   The two remaining filters (Channel 3 and 6) serve to discriminate ocean, snow, and ice surfaces in Arctic regions. Hori et al. (2006) have shown that the emissivity of snow and ice are rather equal at 10.6 µm, but differ significantly at wavelengths close to 12 µm. Furthermore, those differences at wavelengths close to 12 µm are a function of the particular type of snow and ice (e.g., variable grain size).

     The non-imaging infrared thermometer has a larger and more sensitive detector, reducing the measurement uncertainty compared to the TIR imager. With a spectral window between 9.6 and 11.5 µm, the infrared thermometer can serve as a reference for channel 3 of the TIR imager (Table 2). Therefore, it allows measurement comparison between instruments and cross-calibration checks.

2.2   Airborne operation and installation on HALO

VELOX is currently mounted in the belly pod of HALO, outside the aircraft's pressurized cabin. To operate the sensors under constant environmental conditions and minimize thermal effects on the sensor sensitivity, the TIR imager and the infrared thermometer are installed in a temperature and pressure controlled housing. Humidity inside the housing is minimized by purging the inner air volume with nitrogen gas before each flight. However, the temperature control is only unidirectional, using the instrument's heat production and additional heaters but no Peltier cooling system. To monitor the remaining changes of the environmental conditions inside the chamber, six temperature sensors, an air-pressure sensor, and a humidity sensor are installed, measuring with 1 Hz and relative uncertainties of $\pm\,0.1°$C, $\pm\,2.5$ hPa, and $\pm\,2\,\%$, respectively.
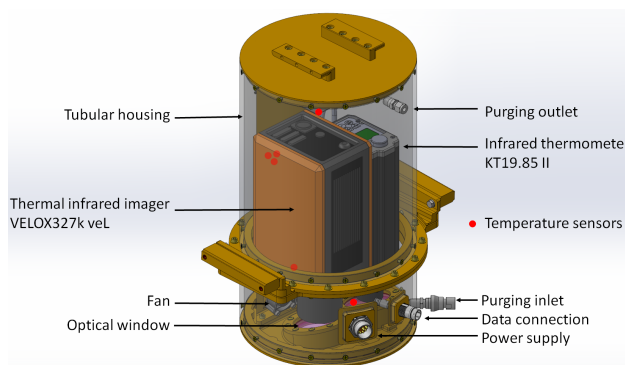
Figure 1. Sketch of the cylindrical housing of VELOX. Only the main components of the system are labeled.

Figure 1 shows a technical sketch with an inside view of the single instruments. This cylindrical housing was manufactured mainly out of aluminum and stainless steel and is 44 cm tall with a diameter of 25.5 cm. The entire setup has a weight of approximately 20 kg.

The TIR imager and the infrared thermometer view through the downward looking side of the cylinder, where optically

130 transparent windows are integrated. As a trade-off between stability and potential effects on the measurement, two separate Germanium windows of 0.5 cm thickness were chosen. The windows provide a high mean transmissivity $\mathcal{T}$ of 0.9395 for the wavelength range between 7.7 μm and 12 μm. Both sides of the window are covered with an anti-reflection coating to minimize transmission losses and specular reflections inside the housing. In addition, the window plane is tilted by 5° with respect to the TIR imager and infrared thermometer viewing axis. This avoids a direct mirroring of the cold detector itself. The remaining

135 reflections are mostly driven by the thermal emission of the imager optics and are imprinted as a homogeneous offset in the measured radiation field. By knowing the temperature of the instrument's optic and the reflection coefficient of the window, these offsets can be removed (see Sect. 3.2.5).

The window is directly exposed to the air flow around the aircraft and cools down significantly more compared to the atmosphere inside of the VELOX cylinder. Condensation or icing on the inside of the window is avoided by several means.

140 The purging with nitrogen gas reduces the absolute humidity to less than $2\,\mathrm{g\,m^{-3}}$. Furthermore, three heating elements are installed, and three fans generate a continuous airflow over the windows.

3 Characterization of the TIR imager

3.1 Geometric characterization

The geometric characterization of the VELOX system addresses two main issues: (i) the relative pixel position and size within

145 the images as a function of aircraft movement and altitude, including the relative position of the field of view (FOV) of the infrared thermometer within the images of the TIR imager, and (ii) the matching procedure of images with different filters.

3.1.1 Viewing geometry

The pixel orientation with respect to the imager's frame (sensor zenith and azimuth angle) is calculated from the detector characteristics (pixel number, detector size) and the imager optics (focal length). The sensor zenith angle is defined as zero in the center of the image and increases towards the sides, reaching $\pm 17.5°$ in the across-track direction and $\pm 14°$ in the direction of flight. The sensor azimuth angle is defined in the mathematically positive direction, with $0°$ in the backward direction.

To evaluate the linearity of the pixel orientation, a laboratory calibration following the chessboard approach (compare, Jäkel et al., 2017) was performed by the use of a black body. The calibration showed that the linear calibration of the pixel zenith and azimuth angle is within a $< 1°$ accuracy.

During data processing, the VELOX images are converted from the airborne-fixed coordinate system into an Earth-fixed coordinate system. The attitude angles of HALO were obtained by the aircraft inertial navigation system. Offsets from the installation of VELOX with respect to the navigation system have been quantified by an inclinometer internally installed in VELOX during test measurements on the ground. During EUREC^{4}A, these offsets were below $1°$ and were implemented into the coordinate transformation.

For a target distance of 10 km, the FOV of VELOX translates into an image size of 6.4 km by 5.1 km with an approximated pixel size of 10 m by 10 m. For the same target distance, the infrared thermometer (FOV = 2.3°) covers a circular spot with 400 m diameter.

The relative position of the infrared thermometer spot within the images of the TIR imager is identified by calculating the correlation between time series of the infrared thermometer with time series of all TIR imager pixels. The TIR imager pixels with the highest correlations identify the position and size of the infrared thermometer spot in the TIR images, which was found to be shifted by $2.86°$ (approximately 500 m at a distance of 10 km) to the right of the nadir direction with respect to the flight direction.

3.1.2 Image shift due to different filters

Although the spectral filters are intended to have a plane surface, even small deviations from this flatness will affect the path of radiation and the focus/mapping of the images on the detector. Therefore, each filter may have a slightly shifted FOV. This needs to be considered during data evaluation, especially when images of different channels are combined. Due to the fixed position of the filters in the filter wheel, this shift stays fixed as long as the filters are not removed or replaced.

In laboratory measurements, these shifts were quantified to be less than 10 pixels in either direction. However, to provide a consistent data set for all channels, only the image parts that were covered by all channels were considered in the final data product. After acquiring an image for each channel, all parts of the scene are identified that are covered by each image. Pixels detecting areas outside this identified scene are removed from the image. Afterwards, all images are slightly smaller, but show perfectly overlapping scenes.

3.2 Radiometric calibrations and corrections

Each pixel of the TIR imager provides a digital number, which is proportional to detected photon counts per unit time. During
EUREC[4]A, the imager was operated with a frame rate of $100\,\mathrm{Hz}$ and an integration time of $70\,\mathrm{\mu s}$. To convert the digital counts
into radiance $I^{\uparrow}$ (in units of $\mathrm{W\,m^{-2}\,nm^{-1}\,sr^{-1}}$) or brightness temperature T_{B} (here, given in units of $^{\circ}\mathrm{C}$, while T_{B} differences
are given in units of K), several calibration and correction processes are applied. This includes a radiometric calibration,
non-uniform corrections of the detector, extended radiometric cross-calibrations, bad-pixel corrections, and corrections of the
influence of the window in the case of airborne application in the tubular mounting. Figure 2 shows an example measurement,
acquired during EUREC[4]A. Each step of the calibration and correction process is displayed in a single panel and is separately
discussed step by step in the subsequent sections.

3.2.1 Internal radiometric calibration model

The TIR imager is provided with an advanced internal radiometric calibration model. This includes calibration factors to
transfer the raw counts into brightness temperature or radiance. It also includes internal corrections with respect to changes in
the environmental, optics, and filter temperatures. This is important, since during research flights those parameters are often
different from the measurement conditions during the initial radiometric characterization of the imager in the laboratory. Using
cross-calibrations in a later step (Sect. 3.2.3), this advanced calibration model is adjusted to the conditions during the research
flights.

Figure 2b shows the image after the internal manufacturers radiometric calibration model was applied to the raw image of
Fig. 2a. It is obvious that after this processing step, artifacts are still imprinted in the image, e.g., regular vertical stripes, which
require further treatment.

3.2.2 Non-uniformity correction

TIR imagers with actively cooled detectors typically suffer from the Narcissus effect, which describes the contamination of the
image by internal reflections of the sensor on the lens (Lau et al., 1977). Furthermore, the ground potential of each detector
pixel has no fixed value. It changes slightly after each restart of the imager, which naturally imprints noise into the measured
images. To remove these effects, a two-point non-uniform correction (NUC, Budzier and Gerlach, 2015) was applied prior
to each flight. The NUC homogenizes all single detector pixels among each other by detecting the variable ground potentials,
which are then applied as a new baseline.

The NUC is generated after the sensor reaches its stable operating temperature. It requires at least two measurements of
a homogeneous target providing different intensities to determine the gain and offset of each pixel. This can be provided either
by a black body set to two different temperatures or by using two different integration times, which artificially change the
intensity recorded by the sensor. During EUREC[4]A, the latter option was chosen. One set of images per channel was recorded
with a low integration time of $10\,\mathrm{\mu s}$ (low radiance, simulating a cold target) and a second one with a higher integration time
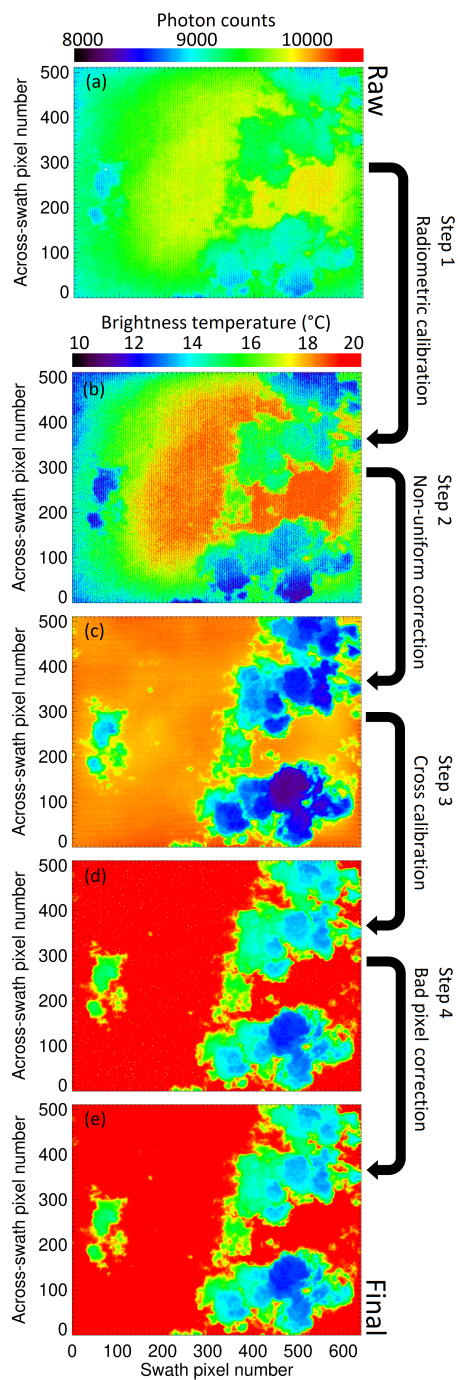
Figure 2. Illustration of the post processing steps using a 2D VELOX image acquired with the broadband channel (7.7 – 12 μm) during the EUREC[4]A flight on 13 February 2020 at 11:37:30 UTC.

of 200 μs (high radiance, simulating a hot target). The measurements were then performed with an integration time in between
these maximum and minimum integration times (70 μs during EUREC⁴A).

Figure 2c shows the resulting image after applying the internal radiometric calibration model and the NUC, which significantly reduced the noise of the image.

3.2.3 Radiometric cross-calibration for field operation

To adapt the internal calibration model of the TIR imager to the environmental conditions during the research flights, cross-calibrations are performed with a black body. In the laboratory, the black body was set to a temperature range comparable to the observations during EUREC⁴A. The environmental conditions (comparable filter and instrument internal temperature) in the laboratory were controlled to be similar to the flight conditions.

By operating VELOX without the window of the mounting tube, cross calibration factors are calculated by comparing pairs of the observed brightness temperature and the true brightness temperature generated by the black body. Tests at different environmental and target temperatures have shown that this adjustment is in a range of less than 1 K.

Figure 2d shows the effect of the cross calibration. Compared to Fig. 2c, the brightness temperature is higher, which indicates the removal of a negative bias by the cross calibration.

3.2.4 Bad-pixel replacement

Most of the noise from the raw images is removed by applying the NUC. However, a second source for noise in the images is bad pixels (Budzier and Gerlach, 2015), which are caused by the manufacturing process of the sensor and the degeneration of the detector with time. Therefore, corrupt pixels are determined in the laboratory by directing the imager on a uniformly tempered black body. Pixels that show values exceeding the two times sigma variability of the entire image are classified as bad pixels. During the image processing, the bad pixels are replaced by the weighted average value determined by their four neighboring pixels.

Figure 2e shows the image after all bad pixels have been replaced. Although the total amount of bad pixels is low ($< 0.5\,\%$ of total pixel), the correction significantly reduces the remaining noise.

3.2.5 Correction of window influence during airborne operation

For the airborne operation of VELOX in the tubular mounting, the effects of the window additionally need to be corrected. In this case, the observations are affected by transmission, absorption/emission, and reflection off/on the window surface. Transmission losses reduce the raw signal, while emission from the window and reflection on the window will increase it. Typically, the window is cooled down by the outer environment, which leads to a difference between the emission by the window (low temperature) and the reflected emission by the imager optics and internal housing (higher temperature).

The radiance $I_{\mathrm{meas}}^{\uparrow}$ at flight altitude, which impinges on the outside of the window, will be mostly transmitted and the remaining fraction will be reflected or absorbed. Re-emission of absorbed radiation by the window occurs due to its own
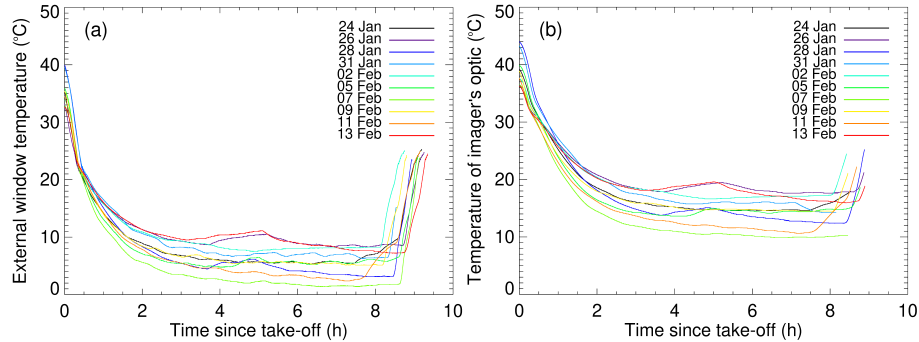
Figure 3. Time series of **(a)** the window temperature and **(b)** the temperature of the imager optics acquired during different EUREC^{4}A research flights.

temperature T_{win}. The resulting radiance $I_{\text{meas}}^{\uparrow}$ behind the window is then composed of the transmitted radiation and the emitted radiation by one side of the window but also by reflected radiation, emitted from the imager optics. According to this, the following equation is applied for the correction of the measured signal:

$$I_{\text{cor}}^{\uparrow} = \frac{I_{\text{meas}}^{\uparrow} - \epsilon_{\text{win}} \cdot I_{\text{win}}(T_{\text{win}}) - \epsilon_{\text{opt}} \cdot I_{\text{opt}}(T_{\text{opt}}) \cdot \mathcal{R}_{\text{win}}}{\mathcal{T}_{\text{win}}}, \tag{1}$$

where $I_{\text{cor}}^{\uparrow}$ is the corrected signal, using $I_{\text{meas}}^{\uparrow}$ as input for the measured signal. The specific absorption/emission is given by ϵ, the reflection by $\mathcal{R}$, and the transmission by $\mathcal{T}$. The subscripts denote if the coefficient belongs to the window (win) or the imager optics (opt). The window temperature is observed by a PT-100 temperature sensor attached to a part of the window that is not covered by the imagers FOV. It is displayed as a color-coded time series for the single flights in Fig. 3a. The optics temperature is stored internally by the imager and is displayed in Fig. 3b. Both show a dependence on flight altitude and environmental temperature, which has a significant time lag. For the first two hours of each flight, the airflow around HALO continues cooling down VELOX. However, once HALO has reached a stable flight altitude, the temperature changes remain small.

The Germanium window has a high average transmissivity of 93.95 % in the wavelength range from 7.7 µm to 12 µm. The spectral behavior of the reflection coefficient is rather constant over the whole range and reaches 5 % on average, while the absorption/emission coefficient is almost negligible over most of the VELOX spectral range but becomes important for the longer wavelengths (≈ 5 % for Channel 5 and 6).

3.3 Sensitivity and stability

A typical measure for the accuracy of measurements in the TIR wavelength range is the Noise Equivalent Temperature Difference (NETD). For the stand alone TIR imager, the manufacturer reports the NETD to be 40 mK. For the full setup, including spectral filters and the window, the NETD was estimated for each channel by measurements in front of a black body. The

260   measurements are started after a two-hour spin up time to guarantee a stabilized filter and instrument operating temperature. Afterwards, 64 subsequent images at 10°C, 128 subsequent images at 20°C, and 64 subsequent images at 30°C were recorded. The difference between the average counts per pixel measured at 30°C and 10°C divided by 20 gives a counts-response file per degree Kelvin. From the 128 images measured at 20°C, the standard deviation of each pixel is calculated leading to a temporal noise file. Dividing the temporal noise file by the response file, averaging over all pixels, and multiplying it by 1000 gives the

265   NETD in mK. The acquired NETDs are 48 mK for the two broadband channels (Channels 1 and 4), 347 mK for Channel 2, 605 mK for Channel 3, 473 mK for Channel 5, and 442 mK for Channel 6. Due to the use of the spectral filters, the detector receives less radiation but is limited by the same thermal noise leading to the partly large NETDs. However, as long as the image has significant contrast, the influence on the accuracy of the measurements remains small.

      To quantify the absolute accuracy, 5 min image sequences were recorded, each using a different black-body temperature
270   setting (5 K steps, -10 °C to 35 °C). Figure 4 shows box and whisker plots calculated from the mean measured brightness temperature of each single image for all six channels. On average, the measured brightness temperature matches well with the black body generated temperature values. Furthermore, a comparison of the single sections reveals that the standard deviation is rather independent of the target temperature (no temperature-dependent trend in the boxes and whiskers).
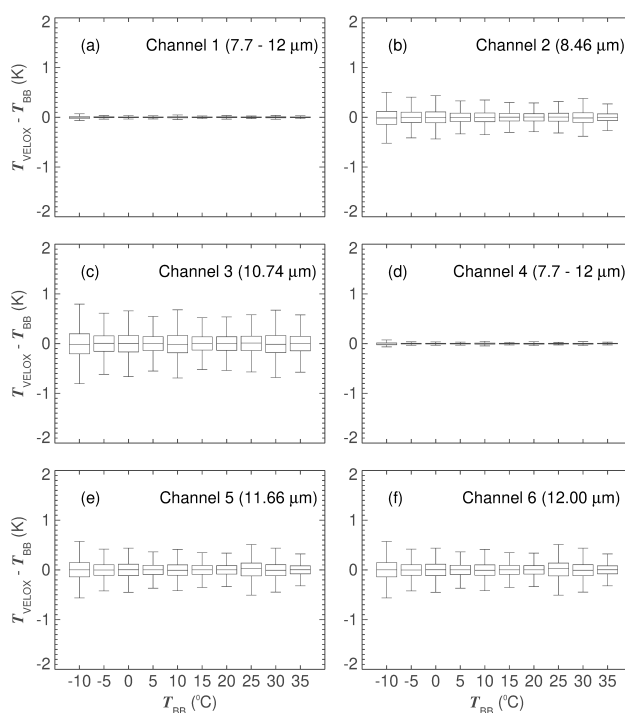
Figure 4. Box and whisker plots for each of the six channels of the TIR imager. Each panel, **(a)** to **(f)**, shows the deviations of the measured brightness temperature (T_{VELOX}) of the single channels from the different black body temperature settings (T_{BB}). The box encloses the interquartile range, defined at 25th and 75th percentile. The whiskers extend out to 1.5 times either the 25th or 75th percentile.

Averaged over the whole time series including all ten black body temperature settings, a standard deviation of 0.016 K is
275   derived for both broadband channels. For the four other channels, the standard deviations are larger with 0.14 K for Channel 2,
0.23 K for Channel 3, 0.17 K for Channel 5, and 0.16 K for Channel 6. However, considering the 25th and 75th percentiles only,
the deviations are in the range of $\pm$ 0.01 K for the two broadband channels, $\pm$ 0.09 K for Channel 2, $\pm$ 0.15 K for Channel 3,
$\pm$ 0.11 K for Channel 5, and $\pm$ 0.1 K for Channel 6.

4   Measurement examples

280   During EUREC[4]A, VELOX was operated during 13 research flights leading to a total recording time of 104 hours, which results
in approximately 82,000 km of horizontal cloud observations. These raw data have been filtered for data quality, resulting in
85 hours (67,000 km) of suitable recordings.

Brightness temperatures measured by VELOX provide the potential for a large number of applications in remote sensing of
the atmosphere and surface. A first set of basic retrieval products is presented in the following sections, including the cloud
285   fraction and cloud top altitude.

4.1   Brightness temperature

Figure 5 displays time series of the averaged brightness temperature of the central 10 by 10 pixels (black) measured with
the different channels of VELOX along the flight track on 13 February 2020. The highest values of the particular brightness
temperature along the time series are related to cloud-free areas below HALO, indicating the detection of the brightness
290   temperature of the ocean surface. All lower values are related to observations of the colder clouds.

Cloud-free simulations (red, see Appendix A) are used to validate the brightness temperature measurements for cloud-free
areas. It can be nicely seen that the highest brightness temperature values along the flight track match the cloud-free simulations.

Figure 6 shows the correlation between the cloud-free simulations and the maximum brightness temperature values classified
by a maximum envelope fit for all six channels. The maximum envelope fit is based on the time series of the averaged brightness
295   temperature of the central 10 by 10 spatial pixels. The time series is divided into sections of 60 seconds, which was found to
be the best setting for trade wind clouds. For each section, the maximum brightness temperature is used to build the envelope
by setting all measurements to this maximum value. In case, no cloud-free ocean was observed in this 60 seconds sequence,
the maximum values of the previous sequence were used. It should be noted that this approach works well only for the trade
wind cumuli analyzed here, but may fail for more stratiform cloud types.

300   The correlation between the measurements and simulations is 0.84 (Pearson correlation). The reason for observed differences
is mainly linked to the spatial/temporal resolution of the simulations, which are limited by the frequency of dropsonde releases
($\approx$ 10 min). Within such a period, the simulations remain constant, while in reality, the atmosphere might change continuously.
However, none of the six channels show a significant deviation from the general correlation. This indicates that the wavelength-
dependent window transmissivity is well captured by the correction.
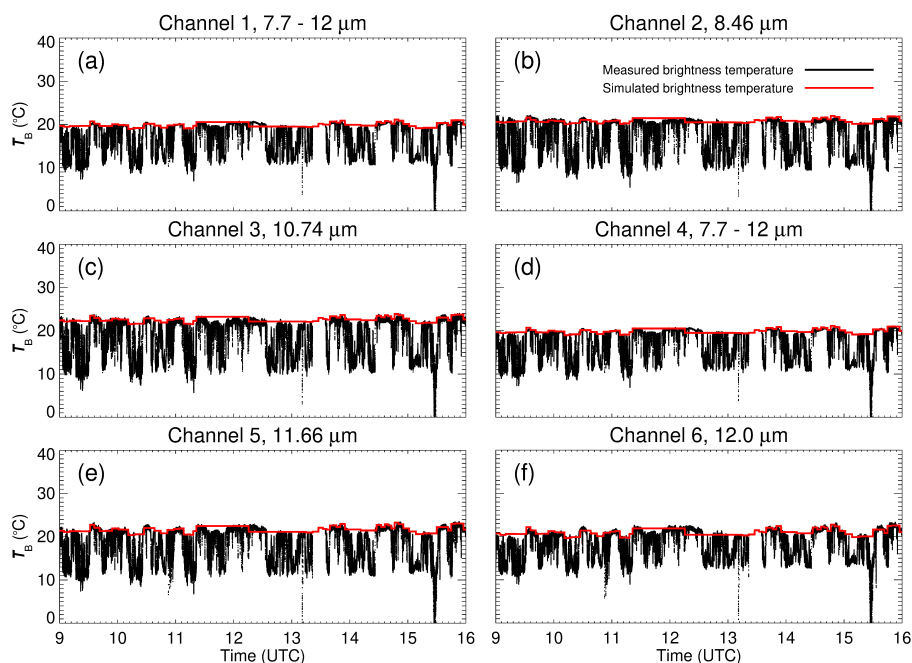
Figure 5. Time series of brightness temperature observed by the central 10 by 10 pixels of VELOX during the EUREC^{4}A flight on 13 February 2020. Each panel, **(a)** to **(f)**, displays the brightness temperature observed by the use of the different channels (black) and the corresponding cloud-free simulations (red).
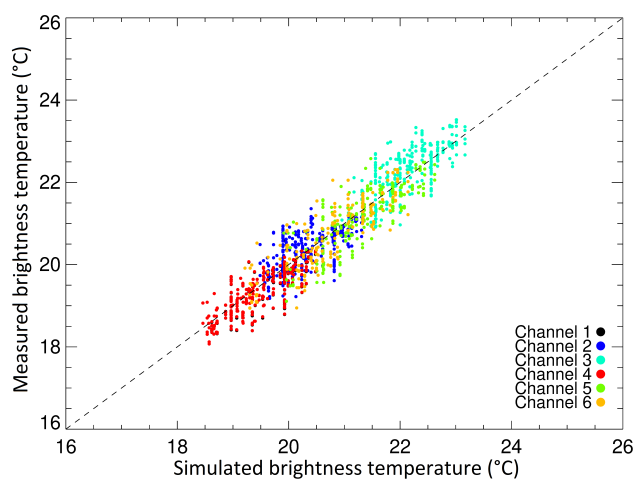
Figure 6. Correlation between the cloud-free simulations and the maximum brightness temperature values displayed in Fig. 5, which represent cloud-free measurements over the warm ocean.

305   Figure 7 shows a series of 2D images of brightness temperature acquired by the broadband channel (Channel 1, 7.7 –12 μm) of VELOX during the EUREC^{4}A flight on 5 February 2020. With HALO flying at 10 km altitude, the images cover an area

of 6.4 km by 5.1 km with a spatial resolution of 10 m by 10 m, both with respect to the surface. The images show the contrast between the warm ocean in red colors and the colder clouds in blue colors and highlight that VELOX is capable of resolving cloud structures with sizes well below 100 m. This is especially beneficial for observations in the trade wind region, where

310 Schnitt et al. (2017) reported that 70 % of all observed clouds have a horizontal extension smaller than 2 km.

VELOX is measuring with a frequency of 100 Hz. Therefore, each sequence of six channels is repeated after 0.06 sec, which translates into a flight distance of approximately 13 m for a typical flight speed of 220 m s^{-1}. This means that subsequent images overlap as illustrated in Fig 7a and b. This overlap depends on the flight speed and the distance to the target. For the example shown in Fig. 7a and b, almost no shift of the scene is visible because 99.5 % of the scene is covered in both images.

315 Therefore, Fig. 7c shows the acquired scene 1 sec later. Here, the shift becomes visible, but 91 % of the image overlaps with Fig. 7a. Such image sequences have potential for stereoscopic 3D reconstruction of clouds (Kölling et al., 2019).

For comparison with traditional pushbroom imagers (specMACS; Ewald et al., 2015) or nadir pointing active remote sensing (WALES, HAMP; Wirth et al., 2009; Mech et al., 2014; Konow et al., 2019), the VELOX data was converted into a pushbroom-like data set by extracting the central swath of each image along the flight path.
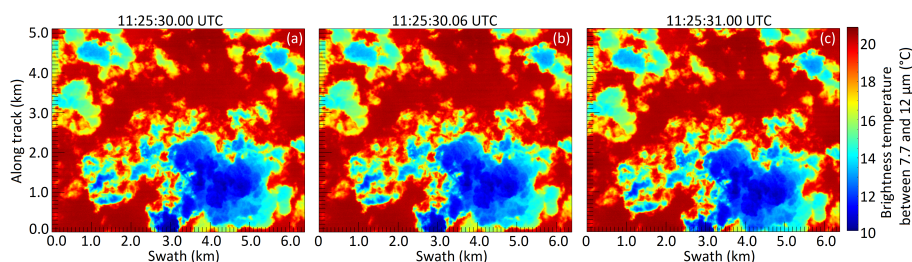
Figure 7. Two-dimensional fields of brightness temperature measured at a flight altitude of approximately 10 km with the VELOX broadband channel between 7.7 μm and 12 μm during the EUREC^{4}A field campaign on 5 February 2020 at **(a)** 11:25:30.00 UTC, **(b)** 11:25:30.06 UTC, and **(c)** 11:25:31.00 UTC.

320 Figure 8 shows a pushbroom image of brightness temperature measured at channel 1 for a 5 min time period on 5 February 2020. The scene covers the single images, which are shown in Fig. 7 and marked here by a black rectangle. Comparing the real 2D images with the pushbroom-like images may indicate if fast moving clouds are distorted in the pushbroom view, which might have consequences for determining the cloud fraction from push-broom images (Konow et al., 2021).

4.2 Cloud cover

325 If the contrast between cloud top temperature and surface temperature is sufficiently high, TIR images are suitable for determining a cloud mask and to estimate the cloud fraction of a scene. In the case of measurements above open ocean, the cloud mask can be determined by a threshold method. During EUREC^{4}A, the ocean had a rather uniform horizontal temperature distribution at about 27 ± 1°C and provides a good background to identify even small and thin clouds. Even a slightly colder brightness temperature can identify a cloud. However, due to atmospheric absorption and emission, the brightness temperature
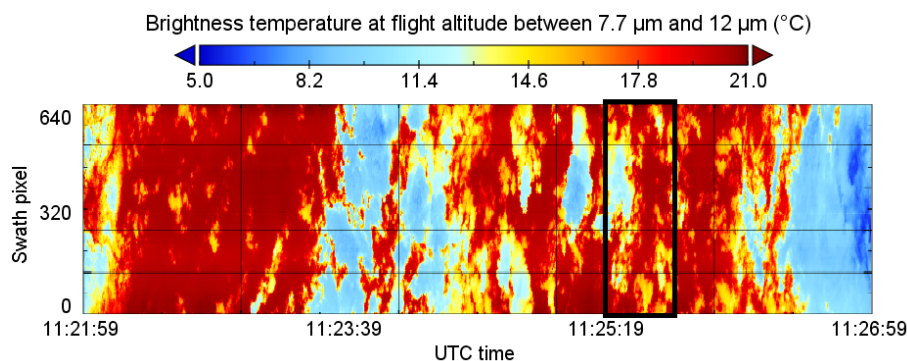
Figure 8. Two-dimensional time series of measured brightness temperature at a flight altitude of approximately 10 km using the center swath line of the VELOX broadband channel (7.7 μm to 12 μm). The data were acquired during the EUREC[4]A field campaign on 5 February 2020 between 11:22:00 UTC and 11:27:00 UTC. The black rectangle marks the measured area displayed in Fig. 7. Adapted from Konow et al. (2021).

.

330 of the ocean surface measured at the flight altitude of about 10 km is lower than the real ocean skin temperature. As the atmospheric conditions along the flight track can change, this needs to be considered when deriving the cloud mask by simple threshold methods. For example, for the flight on 9 February 2020, the measured brightness temperature of the cloud-free ocean varied between 19°C and 21°C (at 10 km flight altitude). To account for such fluctuations of the background brightness temperature, the envelope method described in Sect. 4.1 is applied to continuously adapt the cloud mask algorithm to changes

335 in the atmosphere and ocean conditions by the maximum measured brightness temperature in the surroundings of the particular point of interest. For the cloud-mask algorithm, the difference between the measured brightness temperature and the envelope is calculated.

Figure 9a shows an example of such a time series. The reference level for measurement over cloud-free ocean is constant for the entire flight (Fig. 9b). Thus, a single threshold decides if a cloud was present or not. To account for the fuzzy nature

340 of cloud edges, four different thresholds of 0.5 K, 1.0 K, 1.5 K, and 2.0 K were applied. For the flight shown in Fig. 9, this approach results in a total cloud fraction of 29.4 %, 18.3 %, 15.3 %, and 13.5 % depending on the selected threshold.

Furthermore, the four thresholds were combined into a cloud mask. If the largest threshold of 2 K is exceeded, the measurement is denoted as "most likely cloudy", and if only the lowest threshold of 0.5 K is exceeded, the measurement is denoted as "probably cloudy". The state "cloud free" is classified when no threshold is reached, and "unknown" is classified when the

345 cloud mask algorithm fails, e.g., due to condensation on the window. For the flight shown in Fig. 9, the combined cloud mask identifies 13.6 % of the data as "most likely cloudy", 17.9 % as "probably cloudy", and 68.5 % as cloud free.

The maximum envelope approach was extended to derive the cloud masks from the 2D VELOX images, which allows for the calculation of a cloud fraction for each image. Figure 10a shows the brightness temperature of a 2D VELOX image acquired during the EUREC[4]A flight on 9 February 2020, and Fig. 10b shows the derived, combined cloud mask. It is obvious that the
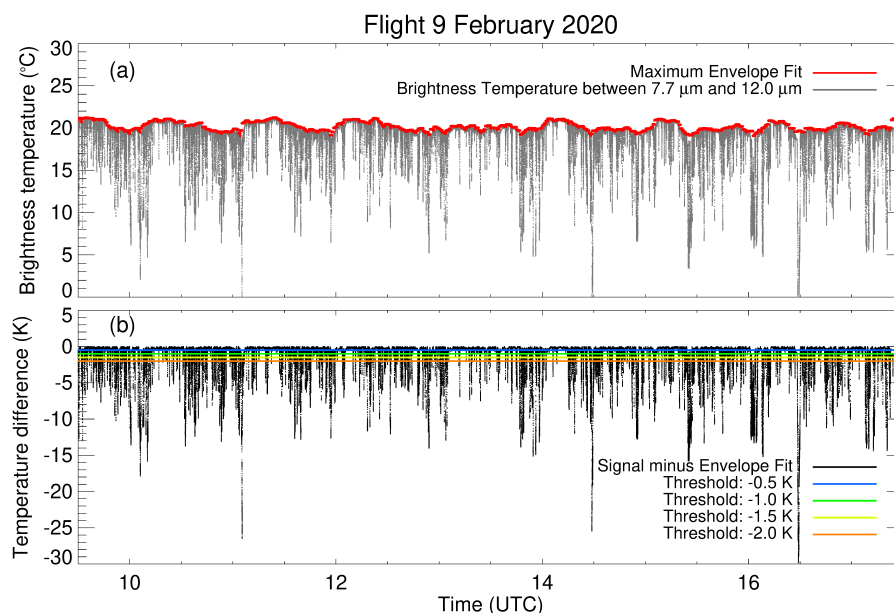
Figure 9. (a) Time series of brightness temperature (black) observed by the central 10 by 10 pixels of VELOX using Channel 1 during the EUREC^{4}A flight on 9 February 2020. The maximum envelope fit is illustrated by the red dots. **(b)** Difference between the measured VELOX brightness temperature and the maximum envelope fit (black). The four thresholds of 0.5 K, 1 K, 1.5 K, and 2.0 K are included by color-coded lines.
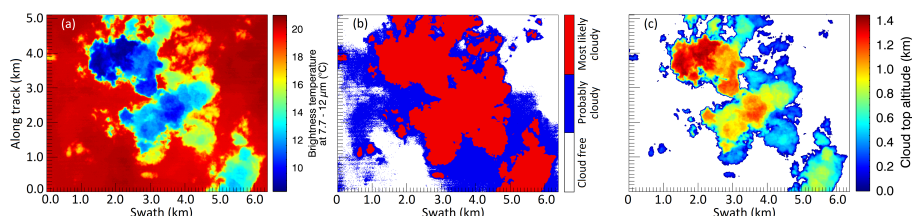
Figure 10. (a) Two-dimensional field of brightness temperature measured at a flight altitude of approximately 10 km with the VELOX broadband channel between 7.7 μm and 12 μm during the EUREC^{4}A field campaign on 9 February 2020 at 15:05:21 UTC. For the same scene, panel **(b)** shows the combined cloud mask and panel **(c)** the retrieved cloud top altitude.

350 cloud mask is also able to detect tiny cloud patches smaller than 100 m in size. By integrating over all pixels in this scene, the cloud cover results in a total amount of 37.2 % "most likely cloudy". The amount of pixels identified as "probably cloudy" is 32.8 % and illustrates the uncertainty of the cloud mask algorithms, which always suffer from the continuous transition of aerosol particles to liquid droplets.

For EUREC^{4}A, time series of the cloud masks and cloud fractions are available for all flights between 24 January and 15

355 February 2020 (Schäfer et al., 2021a, b), which were partly analyzed and compared to other active and passive remote sensing

products by Konow et al. (2021). The comparison highlighted the different sensitivities of the instruments to detect clouds, with VELOX always showing slightly larger cloud fractions compared to the other instruments (Konow et al., 2021). This illustrates the capability of VELOX to also detect small cloud patches. This is a benefit compared to most satellite products, which often suffer from detection limits that miss tiny low clouds (Someya and Imasu, 2018).

4.3 Cloud top altitude

The cloud top temperature measured by VELOX is closely linked to the cloud top altitude. This relation is used by common cloud top altitude retrievals from satellite observations. Here, images from VELOX were used to derive 2D maps of cloud top altitude, which aim to resolve the fine structure of shallow cumulus.

Cloud top altitude retrievals based on TIR brightness temperature need to consider the emission of the atmosphere above the cloud top. Therefore, radiative transfer simulations are performed based on atmospheric profiles measured by dropsondes from HALO (George et al., 2021) to parameterize the temperature offset as a function of the distance to the cloud top.

The effect of the atmosphere was eliminated by an iterative retrieval. The first iteration assumes that the measured brightness temperature scaled by the cloud top emissivity of 0.99 is equal to the cloud top temperature and identifies the cloud top altitude from the atmospheric profile of the radio sounding. This first iteration provides a rough estimate of the distance between cloud top and HALO. Based on this distance, the temperature offset is calculated from the simulation-based parameterization and is added to the measured brightness temperature. This corrected brightness temperature is used in a second iteration step to refine the cloud top altitude. With the NETD of VELOX, this approach allows for the retrieval of cloud top altitudes with a vertical resolution of 40 m. Figure 10c shows the derived cloud top altitude for the cloud scene from 9 February 2020 illustrated in Fig. 10a.

For EUREC[4]A, the cloud top altitudes measured by the central 10 by 10 VELOX nadir pixels were compared to measurements from WALES (Wirth , 2021). Median offsets of up to 470 m were found, which are related to the sometimes large distances to the closest dropsonde used in the simulations. As the active retrieval of WALES is more reliable and available at each point of the flight track, cloud top altitudes of VELOX were cross calibrated to WALES and corrected for these offsets.

5 Conclusions

The technical setup, calibration and correction procedures, and measurement examples of the new airborne TIR imager VELOX (Video airbornE Longwave Observations within siX channels) are presented. VELOX covers six spectral bands in the TIR wavelength range from 7.7 μm to 12.0 μm. It is currently applied on board HALO, but may also be deployed on other airborne platforms or used for ground-based observations. VELOX provides spatially highly resolved 2D fields of upward terrestrial radiance or brightness temperature (FOV of 35.5° by 28.7°, 640 by 512 spatial pixels with 10 m by 10 m pixel size at a target distance of 10 km). The spectral channels were selected to retrieve 2D maps of cloud and surface properties such as cloud cover, cloud top altitude, phase, liquid/ice water path, effective radius, surface temperature, and snow/ice properties.

The post processing of VELOX measurements includes the application of an advanced radiometric calibration model including the effect of the window during airborne observations, non-uniform corrections, cross-calibrations, and bad-pixel corrections. It was shown that additional means beyond the manufacturer calibration are needed to obtain a reliable brightness

390 temperature from the airborne operation of VELOX. A record of the temperature in the tube (of the window and the imager optics) is especially essential to track the thermodynamic behavior of the entire system. The results were validated for cloud-free conditions measured over the ocean using radiative transfer simulations. The uncertainty analysis of the VELOX measurements revealed a high accuracy for the two broadband channels and slightly less accuracy for the other four narrow-band channels, where the detector receives less radiation but is limited by the same thermal noise. The NETD was estimated to be in the range

395 of 48 mK for the broadband channels to 605 mK for Channel 3 and was found to be independent of the target temperature.

First measurements, collected during the EUREC[4]A campaign (Bony et al., 2017; Konow et al., 2021; Stevens et al., 2021) were presented. Two-dimensional images of upward TIR radiance and brightness temperature as well as time series along selected pixels and push-broom-like images were discussed. It was shown that all three methods provide detailed views on clouds and surfaces properties with detected clouds in a horizontal size range below 100 m. To validate the observations,

400 comparisons with radiative transfer simulations were performed, which yield significantly good agreements. Using maximum envelope fits and a threshold method, cloud fractions were calculated, which were then applied to derive a combined cloud mask with confidence levels of "most likely cloudy", "probably cloudy", "cloud free", and "unknown". For the identified cloudy parts, the cloud top temperature was resolved with a thermal resolution of better than 0.1 K, which translates to a resolution of approximately 40 m using basic cloud top altitude retrievals.

405 From the EUREC[4]A campaign, only measurements of warm and liquid low-level trade wind cumuli over a warm ocean surface were available. However, it is envisioned to apply VELOX in three upcoming measurement campaigns; HALO-(AC)[3] operated out of Kiruna, Sweden in March/April 2022 (Wendisch et al., 2021), the EarthCARE Validation Campaign (ECVAL) in 2024, and the Tropical Oceanc and Organized Convection (TOOC) campaign in 2024. These three measurement activities will provide data of different types of clouds (liquid, ice, mixed-phase stratus and convective clouds) in different climatic

410 regions (mid-latitudes, tropics, Arctic). Therefore, the existing products derived from VELOX (brightness temperature, cloud top temperature, cloud top altitude) will be extended to cloud-retrieval products (cloud phase, effective radius, liquid/ice water path) and surface retrievals (sea-surface temperature, snow/ice/water discrimination, snow grain size retrieval). In this sense, the synergy with other instruments deployed on HALO will be very helpful. Therefore, a combined analysis using the different instruments and measurement techniques will be strengthened.

415 *Data availability.* The brightness temperature fields from the TIR imager will be published with a temporal resolution of 1 Hz on the AERIS atmosphere Data and Services Centre (https://en.aeris-data.fr/; last access: 18 November 2021), which is part of the French Data Terra Research Infrastructure. Time series of the infrared thermometer observations are published on the AERIS EUREC[4]A Operational Center (https://observations.ipsl.fr/aeris/eurec4a/#/; last access: 18 November 2021). The cloud mask products from the TIR imager and from the

infrared thermometer are published on AERIS by Schäfer et al. (2021a, b). All other data used and produced in this study are available upon
420   request from the corresponding author (michael.schaefer@uni-leipzig.de).

Appendix A: Cloud-free radiative transfer simulations

To validate and process the measurements obtained with VELOX during EUREC[4]A, radiative transfer simulations are per-
formed along the flight path of HALO (position, altitude, and time) using libRadtran (Emde et al., 2016). Spectral upward
radiance is determined with version two of the DIScrete ORdinaTe (DISORT 2.0) solver (Stamnes et al., 2000) using the 16-
425   stream approximation and is directly converted into brightness temperature. Internally, a spectral resolution of 1 nm is applied
and interpolated on the channel wavelength ranges of VELOX (see Tab. 2). Molecular absorption is considered by the rep-
resentative wavelength approach (REPTRAN), described by Gasteiger et al. (2014). Ozone (O_3) absorption is implemented
and accounts for the strong O_3 absorption band at $9.5\,\mu m$ to $10.5\,\mu m$ wavelength. Merged profiles of radio soundings from the
Barbados Cloud Observatory (BCO, Stevens et al., 2016) with dropsonde measurements from HALO (George et al., 2021)
430   represent the atmospheric conditions above and below the aircraft. For each simulation, the dropsonde closest in time to the
location of HALO was selected. The sea-surface temperature $T_{\rm sea}$, which was rather constant over the EUREC[4]A period, is
set to $300\,K$ ($26.85°C$), according to the observations by the research vessels, e.g., the Maria S Merian or the Ron Brown, the
deployed saildrones, and buoys during the entire campaign.

Author contributions. MS and KW were the primary authors of the paper. BS and MW designed the airborne experiments, which were
435   performed by MS, KW, AE, and MW. The technical work to construct the VELOX system was performed by CH, TR, and FJ. Simulations
with libRadtran were mainly performed by KW, MS, and EJ. MS, KW, AE, and EJ analyzed and compared the observations and simulations.
JT performed the cloud mask analysis, JM the cloud top altitude analysis. AE, MW, EJ, and BS provided technical guidance. All authors
contributed to the interpretation of results and wrote the paper.

Competing interests. The authors declare that they have no conflict of interest.

440   *Acknowledgements.* Very much, we thank the Max Planck Institute for Meteorology, Hamburg, Germany for the funding of the new VELOX
system and providing it to the HALO community. We gratefully acknowledge the funding by the Deutsche Forschungsgemeinschaft (DFG,
German Research Foundation) – Projektnummer 268020496 – TRR 172, within the Transregional Collaborative Research Center "ArctiC
Amplification: Climate Relevant Atmospheric and SurfaCe Processes, and Feedback Mechanisms (AC)[3]. We are further grateful for funding
of the project WE 1900/38-1 by the DFG within the framework of the Priority Programme SPP 1294 to promote research with HALO. Many
445   thanks to the German Aerospace Center (Deutsches Luft und Raumfahrtzentrum, DLR) for the highly appreciated support before, during,
and after the EUREC[4]A campaign.

References

Abrams, M.: The Advanced Spaceborne Thermal Emission and Reflection Radiometer (ASTER): Data products for the high spatial resolution imager on NASA's Terra platform, Int. J. Remote Sens., 21:5, 847-859, DOI: 10.1080/014311600210326, 2000.

450 Bierwirth, E., Ehrlich, A., Wendisch, M., Gayet, J.-F., Gourbeyre, C., Dupuy, R., Herber, A., Neuber, R., and Lampert, A.: Optical thickness and effective radius of Arctic boundary-layer clouds retrieved from airborne nadir and imaging spectrometry, Atmos. Meas. Tech., 6, 1189–1200,https://doi.org/10.5194/amt-6-1189-2013, 2013.

Bony, S., Stevens, B., Ament, F., Bigorre, S., Chazette, P., Crewell, S., Delanoë, J., Emanuel, K., Farrell, D., Flamant, C., Gross, S., Hirsch, L., Karstensen, J., Mayer, B., Nuijens, L., Ruppert, J. H., Sandu, I., Siebesma, P., Speich, S., Szczap, F., Totems, J., Vogel, R., Wendisch, M.,

455 and Wirth, M.: EUREC[4]A: A Field Campaign to Elucidate the Couplings Between Clouds, Convection and Circulation, Surv. Geophys., 38, 1529-1568, DOI: 10.1007/s10712-017-9428-0, 2017.

Brogniez, G., Pietras, C., Legrand, M., Dubuisson, P., and Haeffelin, M.: A High-Accuracy Multiwavelength Radiometer for In Situ Measurements in the Thermal Infrared. Part II: Behavior in Field Experiments, J. Atmos. Oceanic Technol., 20, 1023-1033, doi: 10.1175/1520-0426(2003)20<1023:AHMRFI>2.0.CO;2, 2003.

460 Budzier, H. and Gerlach, G.: Calibration of uncooled thermal infrared cameras, J. Sens. Sens. Syst., 4, 187–197, doi:10.5194/jsss-4-187-2015, 2015.

Cracknell, A.P.: The advanced very high resolution radiometer AVHRR, Oceanographic Literature Review, 5 (44), 526, 1997.

Chylek, P., Robinson, S., Dubey, M. K., King, M. D., Fu, Q., and Clodius, W. B.: Comparison of near-infrared and thermal infrared cloud phase detections, J. Geophys. Res., 111, D20203, doi:10.1029/2006JD007140, 2006.

465 Delanoë, J., and R. J. Hogan: Combined CloudSat-CALIPSO-MODIS retrievals of the properties of ice clouds, J. Geophys. Res., 115, D00H29, doi:10.1029/2009JD012346., 2010.

Delanoë, J., Protat, A., Jourdan, O., Pelon, J., Papazzoni, M., Dupuy, R., Gayet, J. F., and Jouan, C.: Comparison of airborne in situ, airborne radar–lidar, and spaceborne radar–lidar retrievals of polar ice cloud properties sampled during the POLARCAT campaign, J. Atmos. Ocean. Tech., 30, 57–73, doi: 10.1175/JTECH-D-11-00200.1, 2013.

470 Emde, C., Buras-Schnell, R., Kylling, A., Mayer, B., Gasteiger, J., Hamann, U., Kylling, J., Richter, B., Pause, C., Dowling, T., and Bugliaro, L.: The libRadtran software package for radiative transfer calculations (version 2.0.1), Geosci. Model Dev., 9, 1647–1672, doi:10.5194/gmd-9-1647-2016, 2016.

Esaias, W. E., Abbott, M. R., Barton, I., Brown, O. B., Campbell, J. W., Carder, K. L., Clark, D. K., Evans, R., Hoge, F. E., Gordon, H. R., Balch, W. M., Letelier, R., and Minnett, P.: An overview of MODIS capabilities for ocean science observations, IEEE T. Geosci. Remote.,

475 36, 1250-1265, doi:10.1109/36.701076, 1998.

Ewald, F., Kölling, T., Baumgartner, A., Zinner, T., and Mayer, B.: Design and characterization of specMACS, a multipurpose hyperspectral cloud and sky imager, Atmos. Meas. Tech. Discuss., 8, 9853-9925, doi:10.5194/amtd-8-9853-2015, 2015.

Fricke, C., Ehrlich, A., Jäkel, E., Bohn, B., Wirth, M., and Wendisch, M.: Influence of local surface albedo variability and ice crystal shape on passive remote sensing of thin cirrus, Atmos. Chem. Phys., 14, 1943–1958, DOI: 10.5194/acp-14-1943-2014, 2014.

480 Fu, J., Chen, C., Guo, B., Chu, Y., and Zheng, H.: A split-window method to retrieving sea surface temperature from landsat 8 thermal infrared remote sensing data in offshore waters, Estuar. Coast. Shelf S., 236, 106626, doi:10.1016/j.ecss.2020.106626, 2020.

Frey, R. A., Ackermann, S. A., Holz, R. E., Dutcher, S., and Griffith, Z.: The Continuity MODIS-VIIRS Cloud Mask, Remote Sens., 12(20), 3334; doi:10.3390/rs12203334, 2020.

Garnier, A., Pelon, J., Dubuisson, P., Faivre, M., Chomette, O., Pascal, N., and Kratz, D.P.: Retrieval of cloud properties using
485   CALIPSO imaging infrared radiometer. Part I: Effective emissivity and optical depth, J. Appl. Meteorol Climatol., 51, 1407–1425,
        doi:10.1175/JAMC-D-11-0220.1, 2012.

Gasteiger, J., Emde, C., Mayer, B., Buras, R., Buehler, S., and Lemke, O.: Representative wavelengths absorption parameterization applied
        to satellite channels and spectral bands, J. Quant. Spectrosc. Radiat. Transfer, 148, 99–115, doi:10.1016/j.jqsrt.2014.06.024, 2014.

George, G., Stevens, B., Bony, S., Pincus, R., Fairall, C., Schulz, H., Kölling, T., Kalen, Q. T., Klingebiel, M., Konow, H., Lundry, A., Prange,
490   M., and Radtke, J.: JOANNE : Joint dropsonde Observations of the Atmosphere in tropical North atlaNtic meso-scale Environments, Earth
        Syst. Sci. Data Discuss., 1–33, doi:10.5194/essd-2021-162, 2021

Guerin, D. C., Fisher, J., and Graham, E. R.: The enhanced MODIS airborne simulator hyperspectral imager, Proc. SPIE, Algorithms and
        Technologies for Multispectral, Hyperspectral, and Ultraspectral Imagery XVII, 80480L (20 May 2011); doi:10.1117/12.887283, 2011.

Haggerty, J. A., Maslanik, J. A., and Curry, J. A.: Heterogeneity of sea ice surface temperature at SHEBA from aircraft measurements, J.
495   Geophys. Res., 108, C10, 8052, doi:10.1029/2000JC000560, 2003.

Heidinger, A. K., and Pavolonis, M. J.: Gazing at Cirrus Clouds for 25 Years through a Split Window. Part I: Methodology, J. Appl. Meteorol.
        Clim., 48, 1100–1116, doi:10.1175/2008JAMC1882.1, 2009.

Hori, M., Aoki, T., Tanikawa, T., Motoyoshi, H., Hachikubo, A., Sugiura, K., Yasunari, T.J., Eide, H., Storvold, R., Nakajima, Y., and
        Takahashi, F.: In-situ measured spectral directional emissivity of snow and ice in the 8—14 µm atmospheric window, Rem. Sens. Environ.,
500   100, 486–502, doi:10.1016/j.rse.2005.11.001, 2006.

Illingworth, A. J., Barker, H. W., Beljaars, A., Ceccaldi, M., Chepfer, H., Clerbaux, N., Cole, J., Delanoë, J., Domenech, C., Donovan, D.
        P., Fukuda, S., Hirakata, M., Hogan, R. J., Huenerbein, A., Kollias, P., Kubota, T., Nakajima, T., Nakajima, T. Y., Nishizawa, T., Ohno,
        Y., Okamoto, H., Oki, R., Sato, K., Satoh, M., Shephard, M. W., Velázquez-Blázquez, A., Wandinger, U., Wehr, T., and van Zadelhoff,
        G.-J.: The EarthCARE Satellite: The Next Step Forward in Global Measurements of Clouds, Aerosols, Precipitation, and Radiation, B. A.
505   Meteorol. Soc., 96, 1311-1332, doi:10.1175/BAMS-D-12-00227.1, 2015.

Iwabuchi, H., Yamada, S., Katagiri, S., Yang, P., and Okamoto, H.: Radiative and Microphysical Properties of Cirrus Cloud Inferred from
        Infrared Measurements Made by the Moderate Resolution Imaging Spectroradiometer (MODIS). Part I: Retrieval Method, J. Appl. Mete-
        orol. Clim., 53, 1297-1316, https://doi.org/10.1175/JAMC-D-13-0215.1, 2014.

Iwabuchi, H.; Saito, M.; Tokoro, Y.; Putri, N. S., and Sekiguchi, M.: Retrieval of radiative and microphysical properties of clouds from
510   multispectral infrared measurements, Progress in Earth and Planetary Science, 3, 2197-4284, doi:10.1186/s40645-016-0108-3, 2016.

Jäkel, E., Walter, J., and Wendisch, M.: Thermodynamic phase retrieval of convective clouds: impact of sensor viewing geometry and vertical
        distribution of cloud properties, Atmos. Meas. Tech., 6, 539–547, doi:10.5194/amt-6-539-2013, 2013

Jäkel, E., Wendisch, M., Krisna, T. C., Ewald, F., Kölling, T., Jurkat, T., Voigt, C., Cecchini, M. A., Machado, L. A. T., Afchine, A., Costa, A.,
        Krämer, M., Andreae, M. O., Pöschl, U., Rosenfeld, D., and Yuan, T.: Vertical distribution of the particle phase in tropical deep convective
515   clouds as derived from cloud-side reflected solar radiation measurements, Atmos. Chem. Phys., 17, 9049–9066, doi:10.5194/acp-17-9049-
        2017, 2017

Justice, C., O., Román, M., O., Csiszar, I., Vermote, E. F., Wolfe, R. E., Hook, S., J., Friedl, M., Wang, Z., Schaaf, C., B., Miura, T., Tschudi,
        M., Riggs, G., Hall, D., K., Lyapustin, A., I., Devadiga, S., Davidson, C., Masuoka, E., J.: Land and cryosphere products from Suomi NPP
        VIIRS: Overview and status, J. Geophys. Res. Atmos., 118, 9753–9765, doi:10.1002/jgrd.50771, 2013.

520   Kilpatrick, K. A., Podestá, G., Walsh, S., Williams, E., Halliwell, V., Szczodrak, M., Brown, O. B., Minnett, P. J., and Evans, R.: A decade
        of sea surface temperature from MODIS, Remote Sens. Environ., 165, 27-41, doi:10.1016/j.rse.2015.04.023, 2015

Klepp, C., Ament, S., Bakan, S., Hirsch, L., and Stevens, B.: NARVAL Campaign Report, in Reports on Earth System Science, vol. 164 of
ISSN 1614-1199, p. 211, Max Planck Institute for Meteorology Hamburg, Germany, 2014.

Kölling, T., Zinner, T., and Mayer, B.: Aircraft-based stereographic reconstruction of 3-D cloud geometry, Atmos. Meas. Tech., 12,
525   1155–1166, doi:10.5194/amt-12-1155-2019, 2019.

Konow, H. and Jacob, M. and Ament, F. and Crewell, S. and Ewald, F. and Hagen, M. and Hirsch, L. and Jansen, F. and Mech, M. and
Stevens, B.: A unified data set of airborne cloud remote sensing using the HALO Microwave Package (HAMP), Earth Syst. Sci. Data, 11,
921–934, doi:10.5194/essd-11-921-2019, 2019.

Konow, H., Ewald, F., George, G., Jacob, M., Klingebiel, M., Kölling, T., Luebke, A. E., Mieslinger, T., Pörtge, V., Radtke, J., Schäfer, M.,
530   Schulz, H., Vogel, R., Wirth, M., Bony, S., Crewell, S., Ehrlich, A., Forster, L., Giez, A., Groß, S., Gutleben, M., Hagen, M., Hirsch, L.,
Jansen, F., Lang, T., Mayer, B., Mech, M., Prange, M., Schnitt, S., Vial, J., Walbröl, A., Wendisch, M., Wolf, K., Zinner, T., Zöger, M.,
Ament, F., and Stevens, B.: EUREC4A's HALO, Earth Syst. Sci. Data Discuss. [preprint], doi:10.5194/essd-2021-193, in review, 2021.

Krisna, T. C., Wendisch, M., Ehrlich, A., Jäkel, E., Werner, F., Weigel, R., Borrmann, S., Mahnke, S., Pöschl., C., Andreae, M. O., Voigt,
C., and Machado, L. A. T.: Comparing airborne and satellite retrievals of cloud optical thickness and particle effective radius using
535   a spectral radiance ratio technique: two case studies for cirrus and deep convective clouds, Atmos. Chem. Phys., 18, 4439-4462, DOI:
10.5194/acp-18-4439-2018, 2018.

Lau, A. S., Lytle, J. D., and Morrow, H. E. (Eds.): The Narcissus Effect In Infrared Optical Scanning Systems Stray Light Problems in Optical
Systems, SPIE, 0107, 57–62, doi:10.1117/12.964596, 1977.

Libois, Q., Proul, C., Ivanescu, L., Coursol, L., Pelletier, L., S., Bouzid, Y., Barbero, F., Girard, E., and Blanchet, J.-P.: A microbolometer-
540   based far infrared radiometer to study thin ice clouds in the Arctic, Atmos. Meas. Tech., 9, 1817–1832, doi:10.5194/amt-9-1817-2016,
2016.

McMillin, L. M.: The split window retrieval algorithm for sea surface temperature derived from satellite measurements, Adv. Space Res.-
Series, 437–455, doi: 10.1016/b978-0-12-208460-7.50022-4, 1980.

Mech, M., Orlandi, E., Crewell, S., Ament, F., Hirsch, L., Hagen, M., Peters, G., and Stevens, B.: HAMP – the microwave package on the
545   High Altitude and LOng range research aircraft (HALO), Atmos. Meas. Tech., 7, 4539-4553, doi: 10.5194/amt-7-4539-2014, 2014.

Oppelt, N. and Mauser, W.: The Airborne Visible / Infrared Imaging Spectrometer AVIS: Design, Characterization and Calibration, Sensors
(Basel), 2007 Sep 14, 7(9):1934-1953, doi:10.3390/s7091934, 2007.

Parol, F., Buriez, J.C., Brogniez, G., and Fouquart, Y.: Information content of AVHRR channels 4 and 5 with respect to the effective radius
of cirrus cloud particles, J. Appl. Meteorol. 30, 973–984, 1991.

550   Pavolonis, M., J., and Key, J.,R.: Antarctic Cloud Radiative Forcing at the Surface Estimated from the AVHRR Polar Pathfinder and ISCCP
D1 Datasets, 1985–93, J. Appl. Meteorol. Clim. 42, 827–840, doi:10.1175/1520-0450(2003)042<0827:ACRFAT>2.0.CO;2, 2003

Platnick, S.: Vertical photon transport in cloud remote sensing problems, J. Geophys. Res. 105: 22919–22935, 2000.

Platnick, S., Meyer, K. G., King, M. D., Wind, G., Amarasinghe, N., Marchant, B., Arnold, G. T., Zhang, Z., Hubanks, P. A., Holz, R. E.,
Yang, P., Ridgeway, W. L., and Riedi, J.: The MODIS Cloud Optical and Microphysical Products: Collection 6 Updates and Examples
555   From Terra and Aqua, IEEE T. Geosci. Remote., 55, 502–525, doi: 10.1109/TGRS.2016.2610522, 2017.

Schäfer, M., Bierwirth, E., Ehrlich, A., Heyner, F., and Wendisch, M.: Retrieval of cirrus optical thickness and assessment of ice crystal shape
from ground-based imaging spectrometry, Atmos. Meas. Tech., 6, 1855–1868, doi:10.5194/amt-6-1855-2013, 2013.

Schäfer, M., Bierwirth, E., Ehrlich, A., Jäkel, E., Werner, F., and Wendisch, M.: Directional, horizontal inhomogeneities of cloud optical thickness fields retrieved from ground-based and airborne spectral imaging, Atmos. Chem. Phys., 17, 2359–2372, doi:10.5194/acp-17-2359-2017, 2017.

Schäfer, M., Ehrlich, A., Luebke , A., Thoböll , J., Wolf, K., and Wendisch , M.: Two dimensional cloud mask and cloud fraction with 1 Hz temporal resolution derived from VELOX during the EUREC[4]A field campaign, Aeris, doi: 10.25326/163, 2021.

Schäfer, M., Ehrlich, A., Luebke , A., Thoböll , J., Wolf, K., and Wendisch , M.: Cloud mask derived from airborne KT19 measurements during the EUREC[4]A field campaign, Aeris, doi:10.25326/162, 2021.

Schäfler, A., G. Craig, H. Wernli, P. Arbogast, J. Doyle, R. McTaggart-Cowan, J. Methven, G. Rivière, F. Ament, M. Boettcher, M. Bramberger, Q. Cazenave, R. Cotton, S. Crewell, J. Delanoë, A. Dörnbrack, A. Ehrlich, F. Ewald, A. Fix, C. Grams, S. Gray, H. Grob, S. Groß, M. Hagen, B. Harvey, L. Hirsch, M. Jacob, T. Kölling, H. Konow, C. Lemmerz, O. Lux, L. Magnusson, B. Mayer, M. Mech, R. Moore, J. Pelon, J. Quinting, S. Rahm, M. Rapp, M. Rautenhaus, O. Reitebuch, C. Reynolds, H. Sodemann, T. Spengler, G. Vaughan, M. Wendisch, M. Wirth, B. Witschas, K. Wolf, and T. Zinner: The North Atlantic Waveguide and Downstream Impact Experiment, Bull. Amer. Meteor. Soc., doi:10.1175/BAMS-D-17-0003.1, 2018.

Schmit, T. J., Lindstrom, S. S., Gerth, J. J., and Gunshor, M. M.: Applications of the 16 Spectral Bands on the Advanced Baseline Imager (ABI), J. Operational Meteor., 6, 33–46, doi:10.15191/nwajom.2018.0604, 2018.

Schnitt, S., Orlandi, E., Mech, M., Ehrlich, A., and Crewell, S.: Characterization of Water Vapor and Clouds During the Next-Generation Aircraft Remote Sensing for Validation (NARVAL) South Studies, IEEE J. Sel. Top. Appl., 10, 3114–3124, doi:10.1109/JSTARS.2017.2687943, 2017.

Someya, Y. and Imasu, R.: Cloud Screening and Property Retrieval for Hyper-Spectral Thermal Infrared Sounders, Remote Sensing of Aerosols, Clouds, and Precipitation, Chapter 8 - Cloud Screening and Property Retrieval for Hyper-Spectral Thermal Infrared Sounders, Elsevier, 175-187, 2018.

Stamnes, K., Tsay, S.-C., Wiscombe, W., and Laszlo, I.: DISORT, A General-Purpose Fortran Program for Discrete-Ordinate-Method Radiative Transfer in Scattering and Emitting Layered Media: Documentation of Methodology, Dept. of Physics and Engineering Physics, Stevens Institute of Technology, Hoboken, NJ 07030, Dept. of Physics and Engineering Physics, Stevens Institute of Technology, Hoboken, NJ 07030, 2000.

Stevens, B., Farrell, D., Hirsch, L., Jansen, F., Nuijens, L., Serikov, I., Brügmann, B., Forde, M., Linne, H., Lonitz, K., and Prospero, J. M.: The Barbados Cloud Observatory: Anchoring Investigations of Clouds and Circulation on the Edge of the ITCZ, B. Am. Meteorol. Soc., 97, 787–801, doi:10.1175/BAMS-D-14-00247.1, 2016.

Stevens, B, Ament, F., Bony, S., Crewell, S., Ewald, F., Gross, S., Hansen, A., Hirsch, L., Jacob, M., Kölling, T., Konow, H., Mayer, B., Wendisch, M., Wirth, M., Wolf, K., Bakan, S., Bauer-Pfundstein, M., Brueck, M., Delanoë, J., Ehrlich, A., Farrell, D., Forde, M., Gödde, F., Grob, H., Hagen, M., Jäkel, E., Jansen, F., Klepp, C., Klingebiel, M., Mech, M., Peters, G., Rapp, M., Wing, A. A., and Zinner, T.: A high-altitude long-range aircraft configured as a cloud observatory – the NARVAL expeditions, Bull. AMS, 6, 1061-1077. doi: 10.1175/BAMS-D-18-0198.1, 2019.

Stevens, B., Bony, S., Farrell, D., and co-authors: EUREC[4]A, EUREC4A, Earth Syst. Sci. Data Discuss., 1–78, doi:10.5194/essd-2021-18, 2021

Villanueva, D., Senf, F., and Tegen, I.: Hemispheric and Seasonal Contrast in Cloud Thermodynamic Phase From A-Train Spaceborne Instruments, J. Geophys. Res. Atmos., 126, e2020JD034322, doi:10.1029/2020JD034322, 2021

595   Wendisch, M., Handorf, D., Tegen, I., Neggers, R. A. J., and Spreen, G.: Glimpsing the Ins and Outs of the Arctic Atmospheric Cauldron,
         EOS, 102, doi:/10.1029/2021EO155959, 2021

      Wirth, M., Fix. A., Mahnke, P., Schwarzer, H., Schrandt, F., Ehret, G.: The airborne multi-wavelength water vapor differential absorption
         lidar WALES: system design and performance, Applied. Physics B., 96.1, 201–213, doi:10.1007/s00340-009-3365-7, 2009.

      Wirth, M.: Cloud top height derived from airborne measurements with the WALES lidar during the EUREC[4]A field campaign, Aeris,
600   doi:10.25326/216, 2021.

      Wolf, K., A. Ehrlich, M. Jacob, S. Crewell, M. Wirth, and M. Wendisch, 2019: Improvement of airborne retrievals of cloud droplet number
         concentration of trade wind cumulus using a synergetic approach, Atmos. Meas. Tech., 12, 1635–1658, doi:10.5194/amt-12-1635-2019,
         2019.